Preprint version. Published in Computers and Fluids 126, 12-24 (2016)
DOI: 10.1016/j.compfluid.2015.11.012

Optimal control of a transitional jet using a continuous adjoint method

Asim Önder, Johan Meyers*

Department of Mechanical Engineering, KU Leuven, Celestijnenlaan 300A, B3001 Heverlee, Belgium

Abstract

The use of active flow control with unsteady means gains increasing interest in engineering designs. The main bottleneck of the methodology is the strong dependence on trial and error to find the right set of control parameters. In this context, adjoint-based control using high-fidelity simulations is a promising method to explore optimal values in large parameter spaces. However, the applicability of the methodology to complex engineering geometries remains extremely limited. In this work, we employ adjoint-based optimal control using unsteady high-fidelity simulations in a generic unstructured grid framework. To this end, an optimal flow control study is conducted in OpenFOAM® using the continuous adjoint method and DNS simulations. To demonstrate the methodology, we study control of an incompressible axisymmetric jet at $\mathrm{Re}_D = 2000$, with focus on improving its mixing properties. The gradient of the cost functional is calculated with a newly developed unsteady-adjoint solver based on a classical incremental projection scheme. Particular attention is paid into the presentation of mathematical and algorithmic details. Moreover, we address three main issues that remained relatively undiscussed in common practise: the choice of adjoint boundary conditions on computational boundaries, the failure of the adjoint methodology for long optimization horizons in turbulent flows and the treatment of the additional transposed convective term in the adjoint equations. Practical solutions are employed for these issues. Two optimization cases with different initial conditions are designed. To this end, we considered

*Corresponding author

Email addresses: asim.onder@kuleuven.be (Asim Önder), johan.meyers@kuleuven.be (Johan Meyers)

maximization of enstrophy in the near field, for which increments of 10.5% and 5.6% are obtained.
Keywords: turbulent axisymmetric jets, mixing enhancement, DNS, unsteady adjoint solver, OpenFOAM®

1. Introduction

With the experimental visualization of orderly structures in high Reynolds number turbulent flows by pioneering works of Crow and Champagne [1], and Brown and Roshko [2], scientists and engineers dissolved the belief that turbulence is a totally random phenomenon. This new understanding immediately revolutionized flow control strategies. Simple control designs, targeting the mean properties of flows, have been replaced with more sophisticated unsteady methods aiming to manipulate quasi–periodic large–scale coherent motions. This new era in flow control, termed also modern flow control [3], has a huge potential to improve somewhat ated engineering designs using steady active controls or passive geometrical modifications. The main challenge in modern flow control is the lack of predictive methods. Overall progress mainly depends on empirical parametric explorations in large dimensions, as the dynamics of deterministic coherent events and their interaction with random background turbulence is still not very well understood.

Flow optimization methods are efficient tools to explore large parameter spaces in active control of turbulent flows. A typical flow optimization, or optimal flow control study, aims to minimize a cost functional quantifying the flow control objective by using an optimization algorithm and a mathematical flow model. In early efforts, optimal control was successfully applied to boundary layers using simplified flow models such as boundary-layer equations or parabolized stability equations (See, e.g., Refs. [4, 5]). With the increasing availability of computing resources, flow optimization methods using the nonlinear Navier–Stokes equations are establishing themselves as an alternative method in optimal flow control. To date, flow optimization studies using the nonlinear Navier–Stokes equations were carried out almost exclusively with gradient-based methods, as these methods have better convergence properties compared to other classes of optimization algorithms, e.g. evolutionary and

stochastic methods. These methods are based on finding descent directions in the optimization landscape and updating the controls using these descent directions. These directions are constructed from the gradient of the cost functional. Therefore, this gradient has to be calculated at every optimization iteration. To that end, the adjoint method is commonly used, as it provides the whole gradient vector by solving the adjoint Navier-Stokes equations, and is insensitive to the dimension of the control parameter space.

When the adjoint method is applied to unsteady flows using the nonlinear Navier–Stokes equations, it requires the storage of velocity fields at each time step. Early efforts using the adjoint method in combination with DNS or LES suffered due to this excessive storage requirement, and focused on simple canonical flows such as periodic channel flow [6], and spatially developing [7], or convective mixing layers [8]. More recently, optimal control using the adjoint method was applied to reduce jet-noise emisssions using the compressible Navier–Stokes equations, e.g., Marinc and Foysi [9], Schulze et al. [10] and Kim et al. [11]. All these studies investigated turbulent flows in idealized geometries using special high-order discretization methods.

The application of the adjoint methodology on unsteady flows demands further development and testing before it can be employed in engineering problems with complicated geometries. The support for these complex geometries can be achieved only by a transition to generic unstructured CFD frameworks. In recent years, this transition is enabled for steady-flow optimization studies, and optimization with the adjoint method is rapidly emerging to become an industry standard [12, 13, 14, 15, 16]. In these studies, passive control designs have been improved using shape or topology optimization methods that require only a modest description of the flow, e.g. by Reynolds-Averaged Navier–Stokes Equations (RANS). More recently, Carnarius et al. [17] conducted an unsteady adjoint-based control study on unstructured grids by using unsteady RANS in combination with continuous and discrete adjoint method to delay the flow separation on an airfoil by steady blowing or suctioning. However, to date not much experience exists on the use of transient adjoint methods with DNS simulations in generic unstructured CFD frameworks.

In the current work, we perform an adjoint-based optimization study using unsteady high-fidelity turbulent flow simulations in a generic unstructured grid framework. To this end, we have selected the general purpose open-source CFD library OpenFOAM® v2.3.x as the development environment. An incompressible axisymmetric jet at $\mathrm{Re}_D = 2000$ is selected as the application case, and we conduct an optimization study using the continuous adjoint method and DNS simulations to improve the mixing properties of the jet. A steepest-descent algorithm with backtracking line-search is the method of choice for DNS-based optimization. To apply this methodology in OpenFOAM®, the only extension required is the implementation of the unsteady adjoint Navier-Stokes equations. As these equations have a very similar structure to their primal counterparts, maximum code re-usability is possible. The continuous adjoint approach is selected because of this convenience in the implementation. It is often the method of choice in optimal flow control studies with high-fidelity turbulent flow simulations, e.g. [6, 7, 8, 11, 18]. Particular attention is paid to the continuous formulation of the problem and its subsequent discretization. Moreover, we elaborated three main issues in the adjoint-based control of unsteady turbulent flows: the choice of adjoint boundary conditions on computational boundaries, the failure of the adjoint methodology for long optimization horizons in turbulent flows and the treatment of the additional transposed convective term in adjoint equations.

In turbulent jets, increasing the mixing rate between the injected fluid and stagnant ambient fluid is one of the major interests with, e.g., possible applications towards cleaner combustion with less carbon emissions, or more efficient pollutant and waste-water discharge. It can be effectively improved using active flow control with unsteady actuators where the aim is to manipulate dynamic vortical features of the turbulent jet [19]. If unsteady actuators are driven in a regime close to the jet preferred mode, large-scale structures are significantly promoted and the jet spreading is increased [20, 21]. This yields dramatic changes in global mixing characteristics such as the entrainment rate, the decay rate of centreline velocity and passive scalar [22]. However, enhanced coherence in the flow increases the strength and stability of large scale structures and therefore delays their breakdown into smaller

scales [23]. Such a delay yields an inefficient molecular mixing. Therefore, in a mixing augmentation problem, all relevant scales of turbulent motion should be properly addressed by controls. This requires a complicated multi-frequency actuation, as large-scale events occur with characteristic low frequencies, and fine-scale motions are typically observed in high-frequency regimes. Optimal control using high-fidelity turbulent simulations can be very interesting to explore multi-frequency actuation. To our knowledge, the only effort to date in optimal control of jet mixing has been made by Hilgers and Boersma [24]. They maximized the spreading of the jet using stochastic optimization algorithms and DNS simulations. They used in total four control parameters that were amplitude and frequency for helical and axial excitations. Such a low-dimensional optimization problem with a cost function that is mainly sensitive to large-scale motions of the jet clearly addresses large-scale mixing. Up till now, multi-scale mixing behaviour remains relatively unexplored.

The controls in this study are modelled as twelve small hexahedral regions in the domain, that are distributed evenly around the jet circumference with a uniform forcing distribution. Forcing is applied only in the radial direction. Some similarities may exist, e.g., with flap actuators [25], but we selected this type of control mainly for computational reasons (as discussed in detail in Section 2.2). Moreover, radial perturbations are effective in promoting large-scale structures, as the development of primary and secondary vortices in the transition region of a round jet is initiated by the distortions in the azimuthal symmetry of the jet [26, 22]. The signal of controls is designed as a finite Fourier series with 10 frequency components varying between $0.5\mathrm{St}_{pm}$ and $5\mathrm{St}_{pm}$ where St_{pm} is the considered preferred mode frequency with a value of $\mathrm{St}_D = 0.33$. Optimization is carried out for coefficients in the Fourier series, yielding 240 degrees of freedom in the control space. Two optimization cases with different initial conditions are considered. One of the cases contains an additional low magnitude random forcing component in its initial condition. Optimizations are conducted for two different initial conditions up to around ten outer iterations, and reductions of about 10% are obtained. Optimized control signals are found to be composed of additional low value multi-frequency components, and they produce flow fields with enhanced irregularity and

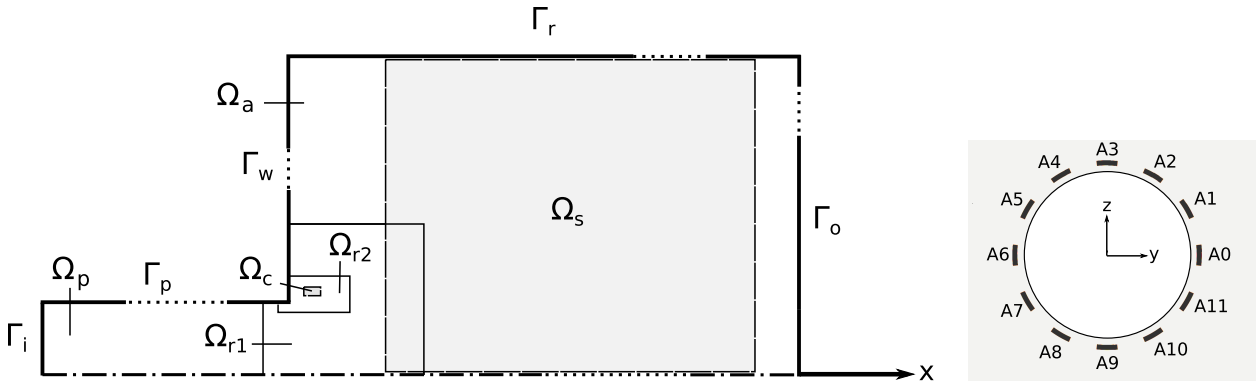

(a) Computational domain (b) Actuators

Figure 1: Geometrical configuration of the optimization problem. (a): Schematic representation of the cylindrical computational domain using an azimuthal cut at $\theta = 0$. Sizes are indicative. (b): Configuration of forcing regions.

mixedness.

The structure of this paper is follows. First, we review the gradient-based optimization with continous adjoint method in detail in Section 2. Then the numerical setting is introduced in Section 3. Subsequently, limitations of the adjoint methodlogy are discussed in Section 4, and results of the optimal control study are presented in Section 5. Finally, conclusions are presented in in Section 6.

2. Optimization with continous adjoint method

In this section, the unsteady jet-flow optimization problem is presented in infinite-dimensional setting.

2.1. Geometrical configuration

Before we present the mathematical details of the jet-flow optimization problem in further sections, we introduce the geometrical details. A descriptive sketch for the three-dimensional computational domain Ω is illustrated in Figure 1a using a two-dimensional cut at $\theta = 0$, and dimensional specifications for various parts in the domain are summarized in Table 1. The computational domain consists of two parts. A large cylindrical domain Ω_a for the ambient

Table 1: Dimensions of the domains in Figure 1 in cylindrical coordinates.

domain	symbol	r/D	θ	x/D
computational domain (ambient)	Ω_a	$[0, 5]$	$[0, 2\pi]$	$[0, 8]$
computational domain (pipe)	Ω_p	$[0, 0.5]$	$[0, 2\pi]$	$[-8, 0]$
observation domain	Ω_s	$[0, 5]$	$[0, 2\pi]$	$[0.6, 6]$
control domain (actuator A0)	Ω_{A0}	$[0.535, 0.565]$	$[-0.07, 0.07]$	$[0.0825, 0.1175]$
grid refinement region (level I)	Ω_{r1}	$[0, 0.8]$	$[0, 2\pi]$	$[-0.2, 1]$
grid refinement region (level II)	Ω_{r2}	$[0.48, 0.6]$	$[0, 2\pi]$	$[0.025, 0.5]$

fluid, which extends $L = 8D$ in the axial direction and $R = 5D$ in the radial direction, is attached to a small pipe domain Ω_p with $R_p = 0.5D$ and $L_p = 8D$. The pipe is introduced to allow adjoint fields to exit the ambient domain while moving upstream with negative convection. The observation domain Ω_s to measure the cost functional in the optimization problem is selected to be $\Omega_s = [0, 5D] \times [0, 2\pi] \times [0.6D, 6D]$, in the radial, azimuthal and axial directions respectively. Additionally, we specify two regions, i.e., Ω_{r1} and Ω_{r2}, to apply higher grid density in the course of discretization. These regions are elaborated in Section 3.3 where we discuss the details of the computational grid.

To control the jet a control domain Ω_c is specified. This domain consists of twelve small hexahedral forcing regions, or actuator, $\Omega_c := \Omega_{A0} \cup \Omega_{A1} \cup \ldots \cup \Omega_{A11}$, that are distributed around the jet circumference. The configuration is illustrated in Figure 1b. Their shape is designed in cylindrical coordinates and the details for an example are given in Table 1 using the actuator *A0*. The center of the actuators is $0.1D$ downstream from the jet inlet plane and $0.55D$ away from the jet axis. A discussion about the selection of these actuators can be found in Section 2.2.

2.2. Cost functional and controls

The first objective in a flow optimization problem is to select a flow characteristic that provides a good measure for the desired flow behaviour, e.g., enhanced mixing in this study.

In order to have a complete view about the mixing properties of the flow, detailed statistical information such as first, second order moments and probability density functions have to be provided [27]. These statistical data can be gathered by averaging over long time series. Such an operation is not possible with the adjoint method considering its excessive storage requirement bottleneck.

Therefore, in the current work, we target instead a kinematical (velocity-based) flow property that is roughly related to small-scale mixing. To this end, we simply choose the total enstrophy integrated over a target region of the domain. Enstrophy is related to total turbulent dissipation, which is mainly associated with small-scale strain [27], and this is essentially responsible for the streching and folding of material elements, a process that also drives mixing [28]. Moreover, Delport et al. [8] demonstrated for a convective mixing layer that maximizing the dissipation accelerates the transition into smaller scales. It is well appreciated that earlier break-up into small scales is beneficial for molecular mixing. Note that other velocity-based cost functionals may also be relevant, e.g., based on the r.m.s value of velocity fluctuations, but these are not further considered in the current work. The cost functional that is employed is therefore:

$$\mathcal{J}_\varepsilon(\boldsymbol{u}) = \frac{1}{2}\int\int_{\overline{\Omega}_s} \omega_i\omega_i \mathrm{d}\boldsymbol{x}\mathrm{d}t, \tag{1}$$

where $\overline{\Omega}_s := \Omega_s \times (0, T]$ is the observation or sensor domain, and $\boldsymbol{\omega} := \nabla \times \boldsymbol{u}$ is the vorticity field.

Now the control design is further elaborated (cf. Figure 1b). Initially, controls were designed as velocity boundary conditions to model zero-net-mass-flux actuation as previously done in Önder & Meyers [22]. However, such a boundary control design can be numerically very challenging to optimize. For a boundary control problem, the gradient of the cost functional reads as follows

$$\nabla\tilde{\mathcal{J}}(\boldsymbol{\phi})_i = \frac{1}{\mathrm{Re}}\frac{\partial\xi_i}{\partial x_j}n_j - qn_i, \qquad \text{on } \partial\Omega_c, \tag{2}$$

$\partial\Omega_c$ is the control boundary, $\boldsymbol{\phi}$ is the control field, $\boldsymbol{\xi}$ is the adjoint velocity field and q is the adjoint pressure field. The reader is referred to Ref. [29] for a derivation. The first

term requires the gradient of the adjoint velocity on the control wall. This gradient can be extremely steep if the controls are placed into the areas where the flow is most sensitive, e.g. close to shear layer in the case of round jets. Therefore, the calculation of this term is error-prone unless an extremely high grid resolution is applied in the vicinity of the wall. Moreover, such a refinement can impose infeasible restrictions on the time step. Furthermore, the second term requires the adjoint pressure on the wall. Segregated solvers such as the projection method used in this work employ an unphysical Neumann boundary condition for the pressure. This unphysical boundary condition yields spurious boundary layers in the pressure. Thus, the calculated pressure on the control boundary is not reliable. Therefore, our choice to use the projection algorithm to impose the incompressible continuity equation, forces us to design a control configuration away from the boundaries. Optimal boundary control of incompressible flows can be tackled in the future, if a modern solver based on the coupled solution of momentum and continuity equations is implemented into OpenFOAM®. We also note that this issue would not exist in compressible flow solvers, where the pressure is determined by an equation of state, and an additional energy equation.

Due to the difficulties related to the computation of the adjoint velocity gradient and adjoint pressure on the control wall, optimal boundary control is not considered in this work. We employed distributed controls instead, which are designed as localized forcing regions that are distributed around the jet circumference, and are capable of introducing azimuthal perturbations. Similar adjoint-based jet control using distributed control was previously employed in noise reduction of round jets [11] and plane jets [9]. However, these studies employed local heat source regions in the domain.

2.3. Optimality conditions

In this section, first, the optimal distributed jet control problem using the enstrophy integral $\mathcal{J}_\varepsilon(\boldsymbol{u})$ in Eq. (1) as cost functional is mathematically formulated. Subsequently, its optimality conditions are presented. No explicit constraints are applied to the controls.

Gunzburger suggests that computational boundaries, e.g. outflow Γ_o and lateral Γ_r boundaries (cf. Figure 1a), should not be included in the derivation of continuous optimality

conditions [30]. These boundary conditions are non-physical, and therefore they are not considered as the part of the continuous problem. Thus, in the presentation of optimality conditions in infinite-dimensional framework, we consider that the jet is ejected into an infinite domain that is bounded by Dirichlet boundaries $\partial\Omega := \Gamma_i \cup \Gamma_w \cup \Gamma_p \cup \Gamma_\infty$. This strategy prevents complicated adjoint boundary conditions that are derived from Neumann boundary conditions in the primal problem. Following the derivation of adjoint equations in the continuous framework we will employ simple Neumann boundary conditions for the adjoint velocity on the computational boundaries as well. We verified this practical selection by benchmarking the adjoint-gradient to finite-difference based gradient in Section 3.4.

In order to bound the controls a penalization is applied. Consequently, the enstrophy maximization problem with Dirichlet boundaries reads as follows

$$\min_{\boldsymbol{u},\boldsymbol{\phi}} \mathcal{J}(\boldsymbol{u},\boldsymbol{\phi}) := -\frac{1}{2}\int\int_{\overline{\Omega}_s} \omega_i\omega_i \mathrm{d}\boldsymbol{x}\mathrm{dt} + \frac{\gamma}{2}\int\int_{\overline{\Omega}_c} \phi_\mathrm{i}\phi_\mathrm{i}\mathrm{d}\boldsymbol{x}\mathrm{dt} \tag{3}$$

s.t.

$$\frac{\partial u_i}{\partial t} + \frac{\partial u_j u_i}{\partial x_j} + \frac{\partial p}{\partial x_i} - \frac{1}{\mathrm{Re}_D}\frac{\partial^2 u_i}{\partial x_j \partial x_j} = f_i \quad \text{in } \overline{\Omega}, \tag{4}$$

$$\frac{\partial u_i}{\partial x_i} = 0 \quad \text{in } \overline{\Omega}, \tag{5}$$

$$f_i = \begin{cases} \phi_i & \text{in } \overline{\Omega}_c \\ 0 & \text{in } \overline{\Omega} \setminus \overline{\Omega}_c \end{cases}, \tag{6}$$

$$u_i = g_i \quad \text{on } \overline{\partial\Omega}, \tag{7}$$

$$u_i = u_i^0 \quad \text{in } \Omega \times \{t = 0\}, \tag{8}$$

where $\overline{(\cdot)}$ notation is used to represent space-time domains, $\overline{\Omega} := \Omega \times (0, T]$ is the flow domain, $\overline{\Omega}_c := \Omega_c \times (0, T]$ is the control domain, $\boldsymbol{\phi}$ is the control field localized in Ω_c, $\boldsymbol{u}$ is the velocity field, p is the pressure field, $\boldsymbol{g}$ is the prescribed velocity values on Dirichlet boundaries and γ is a penalization parameter.

The objective of the optimization problem in Eqs. (3)-(8) is to find $\overline{\boldsymbol{u}}$ and $\overline{\boldsymbol{\phi}}$ such that

$$\mathcal{J}(\overline{\boldsymbol{u}}, \overline{\boldsymbol{\phi}}) < \mathcal{J}(\boldsymbol{u}, \boldsymbol{\phi}) \;\; \forall \boldsymbol{u} \in \mathcal{H}_u, \boldsymbol{\phi} \in \mathcal{H}_c \tag{9}$$

where $\mathcal{H}_u$ and $\mathcal{H}_c$ are appropriate Hilbert spaces.

In order to derive the optimality conditions and find the set of equations that $\overline{\boldsymbol{u}}$ and $\overline{\boldsymbol{\phi}}$ should satisfy, the optimization problem in Eqs. (3)–(8) is first cast into an equivalent unconstrained reduced formulation

$$\min_{\boldsymbol{\phi}} \tilde{\mathcal{J}}(\boldsymbol{\phi}) := -\frac{1}{2}\int\int_{\overline{\Omega}_s} \omega_i(\boldsymbol{\phi})\omega_i(\boldsymbol{\phi})\mathrm{d}\boldsymbol{x}\mathrm{d}t + \frac{\gamma}{2}\int\int_{\overline{\Omega}_c} \phi_i\phi_i\mathrm{d}\boldsymbol{x}\mathrm{d}t \tag{10}$$

with the reduced cost functional $\tilde{\mathcal{J}} : \mathcal{H}_c \to \mathbb{R}$. Subsequently, the reduced cost functional is assumed to be differentiable and its gradient $\nabla\tilde{\mathcal{J}}$ is defined. If $\mathcal{H}_c$ is endowed with the scalar product

$$(\boldsymbol{a}, \boldsymbol{b})_{\mathcal{H}_c} = \int\int_{\overline{\Omega}_c} a_i b_i \mathrm{d}\boldsymbol{x}\mathrm{d}t, \tag{11}$$

then the gradient of the reduced cost functional is defined as the Riesz-representation of the derivative $\tilde{\mathcal{J}}'$ [31], i.e.,

$$\left(\nabla\tilde{\mathcal{J}}, \boldsymbol{\phi'}\right)_{\mathcal{H}_c} = \tilde{\mathcal{J}}'(\boldsymbol{\phi'}) \quad \forall \boldsymbol{\phi'} \in \mathcal{H}_c,$$

where $\tilde{\mathcal{J}}'(\boldsymbol{\phi'})$ is the Gateaux derivative in the direction $\boldsymbol{\phi'}$ given by

$$\tilde{\mathcal{J}}'(\boldsymbol{\phi'}) := \left.\frac{\mathrm{d}}{\mathrm{d}\alpha}\right|_{\alpha=0} \tilde{\mathcal{J}}(\boldsymbol{\phi} + \alpha\boldsymbol{\phi'}) \quad \forall \boldsymbol{\phi'} \in \mathcal{H}_c. \tag{12}$$

Having defined the gradient of the reduced cost functional, the optimality condition can be described. The necessary condition of first order optimality states that an optimal solution $\overline{\boldsymbol{\phi}}$ renders a stationary point such that $\nabla\tilde{\mathcal{J}}(\overline{\boldsymbol{\phi}}) = 0$ [31].

A computational expression can be derived by applying the chain rule to the derivative of the implicit variable $\boldsymbol{u}(\boldsymbol{\phi})$, and then deriving the corresponding adjoint operators. As the final expression contains adjoint states, the adjoint equations have to be derived subsequently [31].

A popular alternative to derive optimality conditions is the formal Lagrange method [32]. In this method, a Lagrangian functional is introduced to the PDE constrained optimization problem, and the optimality conditions are found from the vanishing directional derivatives of the Lagrangian. In the course of the derivation, all the integrals are formally defined

and one would not care if they make sense in a functional analytic setting [32]. Thus, this approach is more attractive for complicated problems and it is commonly employed in the flow optimization studies, e.g. [29, 33, 12]. It is also the method of choice in this section to the derive optimality system of equations. We start the derivation by associating the following Lagrangian to the optimization problem in Eqs. (3)-(8)

$$\begin{aligned}\mathcal{L}(\boldsymbol{u}, p, \boldsymbol{\phi}, \boldsymbol{\xi}, q) &= \mathcal{J}(\boldsymbol{u}, \boldsymbol{\phi}) \\ &+ \int\int_{\overline{\Omega}} \left(\frac{\partial u_i}{\partial t} + \frac{\partial u_j u_i}{\partial x_j} + \frac{\partial p}{\partial x_i} - \frac{1}{\mathrm{Re}_D} \frac{\partial^2 u_i}{\partial x_j \partial x_j} - f_i \right) \xi_i \mathrm{d}\boldsymbol{x}\mathrm{dt} \\ &+ \int\int_{\overline{\Omega}} q \frac{\partial u_i}{\partial x_i} \mathrm{d}\boldsymbol{x}\mathrm{dt}, \end{aligned} \tag{13}$$

where $\boldsymbol{\xi}$ and q are Lagrange multipliers known as adjoint velocity and pressure states. Since the Lagrangian is an unconstrained functional, the first order optimality condition ensures that at the optimal point $(\overline{\boldsymbol{u}}, \overline{p}, \overline{\boldsymbol{\phi}}, \overline{\boldsymbol{\xi}}, \overline{q})$ the directional derivatives of the Lagrangian with respect to states, adjoint states and controls should vanish identically, such that

$$\mathcal{L}_{\boldsymbol{\xi}}(\boldsymbol{\xi'}) = \mathcal{L}_q(q') = 0, \quad \Rightarrow \text{ state equations} \tag{14}$$

$$\mathcal{L}_{\boldsymbol{u}}(\boldsymbol{u'}) = \mathcal{L}_p(p') = 0, \quad \Rightarrow \text{ adjoint equations} \tag{15}$$

$$\mathcal{L}_{\boldsymbol{\phi}}(\boldsymbol{\phi'}) = 0, \quad \Rightarrow \text{ design equations} \tag{16}$$

where the directional derivative, e.g. with respect to velocity $\boldsymbol{u}$ in the direction of $\boldsymbol{u'}$, reads as follows,

$$\mathcal{L}_{.\boldsymbol{u}}(\boldsymbol{u'}) \equiv \left. \frac{\mathrm{d}}{\mathrm{d}\alpha} \right|_{\alpha=0} \mathcal{L}(\boldsymbol{u} + \alpha \boldsymbol{u'}, p, \boldsymbol{\phi}, \boldsymbol{\xi}, q). \tag{17}$$

The conditions in Eqs. (14)-(16) lead the following optimality system

$$\frac{\partial u_i}{\partial t} + \frac{\partial u_j u_i}{\partial x_j} + \frac{\partial p}{\partial x_i} - \frac{1}{\mathrm{Re}_D}\frac{\partial^2 u_i}{\partial x_j \partial x_j} = f_i \quad \text{in } \overline{\Omega}, \tag{18}$$

$$\frac{\partial u_i}{\partial x_i} = 0 \quad \text{in } \overline{\Omega}, \tag{19}$$

$$f_i = \begin{cases} \phi_i & \text{in } \overline{\Omega}_c \\ 0 & \text{in } \overline{\Omega} \setminus \overline{\Omega}_c \end{cases}, \tag{20}$$

$$u_i = g_i \quad \text{on } \overline{\partial\Omega}, \tag{21}$$

$$u_i(0) = u_i^0 \quad \text{in } \Omega, \tag{22}$$

$$-\frac{\partial \xi_i}{\partial t} - u_j\frac{\partial \xi_i}{\partial x_j} + \xi_j\frac{\partial u_j}{\partial x_i} - \frac{\partial q}{\partial x_i} - \frac{1}{\mathrm{Re}_D}\frac{\partial^2 \xi_i}{\partial x_j \partial x_j} = h_i \quad \text{in } \tilde{\Omega}, \tag{23}$$

$$\frac{\partial \xi_i}{\partial x_i} = 0 \quad \text{in } \tilde{\Omega}, \tag{24}$$

$$h_i = \begin{cases} -\dfrac{\partial^2 u_i}{\partial x_j \partial x_j} & \text{in } \tilde{\Omega}_s \\ 0 & \text{in } \tilde{\Omega} \setminus \tilde{\Omega}_s \end{cases}, \tag{25}$$

$$\xi_i = 0 \quad \text{on } \partial\tilde{\Omega}, \tag{26}$$

$$\xi_i = \xi_i^0 = 0 \quad \text{in } \Omega \times \{t = T\}, \tag{27}$$

$$\gamma\phi_i - \xi_i = 0, \quad \text{on } \overline{\Omega}_c. \tag{28}$$

The reader is referred to Ref. [34] for a derivation of this result. Eqs. (18)-(22) are the state equations, Eqs. (23)-(27) are the adjoint equations, and Eq. (28) is the design equation.

In addition to temporal, convective and diffusive terms, the adjoint momentum equation contains an additional term $\xi_j(\partial u_j/\partial x_i)$, will be referred to as *the transposed convection term*. An alternative version for this term can be derived by applying integration by parts on this term [12]. Consequently, an alternative form for the adjoint momentum equation is obtained

$$-\frac{\partial \xi_i}{\partial t} - u_j\frac{\partial \xi_i}{\partial x_j} - u_j\frac{\partial \xi_j}{\partial x_i} - \frac{\partial q}{\partial x_i} - \frac{1}{\mathrm{Re}_D}\frac{\partial^2 \xi_i}{\partial x_j \partial x_j} = h_i \quad \text{in } \tilde{\Omega}, \tag{29}$$

with the alternative form of the transposed convection term $-u_j(\partial \xi_j/\partial x_i)$. The Dirichlet boundary conditions and the initial condition remain unchanged.

2.4. A gradient–based minimizer

The optimality system in Eqs. (18)-(28) is a set of strongly coupled partial differential equations containing nonlinearity. Therefore, it has to be solved iteratively. However, an iterative solution to this coupled system is computationally very demanding considering the size of DNS simulations. Thus, for large-scale turbulence problems, generic optimization algorithms that are designed to minimize the reduced cost functional $\tilde{\mathcal{J}}$, are employed. To this end, first-order gradient-based methods such as the steepest-descent method and the nonlinear conjugate-gradient method are common choices because of their low storage requirements [6, 30].

The method of choice in this study is the steepest descent method with a backtracking line-search. It employs the negative of the reduced gradient to update the control fields every outer iteration. The reduced gradient can be found from the Lagrangian $\mathcal{L}$ as follows

$$\left(\nabla\tilde{\mathcal{J}},\boldsymbol{\phi}'\right)_{\mathcal{H}_c}=\left(\nabla_{\boldsymbol{\phi}}\mathcal{L},\boldsymbol{\phi}'\right)_{\mathcal{H}_c}:=\mathcal{L}_{\boldsymbol{\phi}}(\boldsymbol{\phi}')\quad\forall\boldsymbol{\phi}'\in\mathcal{H}_c. \tag{30}$$

The reader is referred to [32] for a derivation of this result. Using the Eqs. (16) and (28), the reduced gradient is now given by

$$\nabla\tilde{\mathcal{J}}(\boldsymbol{\phi})=\gamma\boldsymbol{\phi}-\boldsymbol{\xi}. \tag{31}$$

Basic steps of the selected steepest descent algorithm for the infinite-dimensional jet optimization is given in Algorithm 1. The norm $\|\cdot\|_{\mathcal{H}_c}$ in the algorithm is found from the scalar product in Eq. (11), i.e.,

$$\|\boldsymbol{\phi}\|_{\mathcal{H}_c}:=\sqrt{(\boldsymbol{\phi},\boldsymbol{\phi})_{\mathcal{H}_c}}\quad\forall\boldsymbol{\phi}\in\mathcal{H}_c. \tag{32}$$

In this study we have selected the following values for the free parameters in the algorithm: $\beta=10^{-4}$, $\kappa=0.1$, and $\eta=0.25$.

3. Numerical details

In Section 2, a jet flow optimization problem and a gradient-based optimization algorithm to solve this problem were introduced. The optimization algorithm was in infinite-

Algorithm 1: The steepest-descent algorithm

I initialization:

i Choose an initial control field $\boldsymbol{\phi}_0$;

ii Solve the state equations in (18)-(22) forward in time with $\boldsymbol{\phi}_0$, and obtain the corresponding state field $\boldsymbol{u}_0$ and functional value $\tilde{\mathcal{J}}(\boldsymbol{\phi}_0)$;

II main optimization loop, i.e. for $m = 1, 2, 3, \ldots$:

i Solve the adjoint equations in (23)-(27) backward in time with $\boldsymbol{u}_{m-1}$ and obtain the adjoint field $\boldsymbol{\xi}_m$;

ii Evaluate the gradient $\nabla\tilde{\mathcal{J}}(\boldsymbol{\phi}_{m-1}) = \gamma\boldsymbol{\phi}_{m-1} - \boldsymbol{\xi}_m$;

iii Set a minimum limit $\tilde{\mathcal{J}}^g$ by Armijo rule [35, 36] to ensure a sufficient decrease, i.e.

$$\tilde{\mathcal{J}}^g = \tilde{\mathcal{J}}(\boldsymbol{\phi}_{m-1}) - \beta\left(\|\nabla\tilde{\mathcal{J}}(\boldsymbol{\phi}_{m-1})\|_{\mathcal{H}_c}\right)^2;$$

iv Set the initial step size $\lambda = \kappa\|\boldsymbol{\phi}_{m-1}\|_{\mathcal{H}_c}$;

v Update the controls $\boldsymbol{\phi}_m = \boldsymbol{\phi}_{m-1} - \lambda\nabla\tilde{\mathcal{J}}(\boldsymbol{\phi}_{m-1})$;

vi Solve the state equations in (18)-(22) forward in time with $\boldsymbol{\phi}_m$, and obtain $\boldsymbol{u}_m$ and $\tilde{\mathcal{J}}(\boldsymbol{\phi}_m)$;

vii If $\tilde{\mathcal{J}}(\boldsymbol{\phi}_m) > \tilde{\mathcal{J}}^g$ set $\lambda = \eta\lambda$ and go to step (v); otherwise, set $m = m + 1$, and go to step (i);

dimensional setting. In this section, the discretization of the optimization problem is discussed. The discretization of the primal equations is not discussed, as it is similar to the discretization of adjoint equations. The reader is referred to Ref. [34] for a detailed presentation of the discretization of primal equations.

3.1. Discretization of the adjoint equations

The open-source library OpenFOAM® is employed in this study (using the v2.3.x distribution). OpenFOAM® employs a collocated Finite-Volume Method (FVM) for the spatial discretization of conservation equations. Detailed information about FVM numerics in OpenFOAM® can be found in Jasak [37]. We employed linear interpolation for the calculation of the convective flux, and a central-differencing scheme for the construction of the diffusive flux. The flux velocities on faces are modified using Rhie–Chow interpolation to prevent velocity-pressure decoupling.

The spatial discretization of the additional transposed convection term $\xi_j(\partial u_j/\partial x_i)$ in adjoint equations is carried out as follows

$$\left(\xi_j \frac{\partial u_j}{\partial x_i}\right)^k \approx \frac{\xi_j^k}{|\Omega_k|} \sum_{f=1}^{N_{kf}} u_j^f n_i^f |\partial\Omega_k^f|, \tag{33}$$

where the superscripts k and f denote evaluations in element and face centroids respectively, $|\Omega_k|$ is the volume of a polyhedral element, $|\Omega_k^f|$ is the area of the element face and n^f its corresponding unit normal, and N_{kf} is the total number of faces around the element. Similar spatial discretization can be applied to the alternative form $-\xi_j(\partial u_j/\partial x_i)$.

OpenFOAM® includes a segregated adjoint solver entitled *adjointShapeOptimizationFoam*, which is based on the work of Othmer [12]. This solver is developed to calculate gradients for shape/topology optimization problems using RANS. Being a steady solver using the SIMPLE scheme, it is not suitable for unsteady problems. An unsteady adjoint solver requires a machinery for backward-in-time stepping with changing velocity fields at every time step. Therefore, a new adjoint solver using the adjoint version of an incremental projection scheme [38, 34] is implemented. The incremental projection scheme is non-iterative, and

therefore costs less than iterative schemes that require multiple pressure-Poisson solutions, e.g., PISO and SIMPLE schemes.

The spatial discretization in Eq. (33) couples the adjoint velocity components. Since OpenFOAM® does not support the coupling of the velocity components at the time of this study, the temporal discretization of the transposed convection term cannot be handled implicitly. Therefore, a second-order Adams–Bashforth scheme is employed to discretize the transposed convection term in time. The rest of terms are integrated in time using a one-step-theta scheme using an implicitness parameter θ. Consequently, an incremental projection scheme using a semi-implicit, i.e. $\theta > 0$, backward in time stepping is formulated in space continuum as follows:

1. Momentum step: Solve for the preliminary adjoint velocity $\tilde{\xi}_i^n$;

$$\frac{\tilde{\xi}_i^{\,n} - \xi_i^{n+1}}{\delta t} + u_j^{n+\theta}\frac{\partial \tilde{\xi}_i^{\,n+\theta}}{\partial x_j} + c_i = \frac{1}{Re_D}\frac{\partial^2 \tilde{\xi}_i^{\,n+\theta}}{\partial x_j \partial x_j} - \frac{\partial q^{n+1}}{\partial x_i} + h_i^n \quad \text{in } \Omega, \tag{34}$$

$$\tilde{\xi}_i^n = g_i^n \quad \text{on } \partial\Omega, \tag{35}$$

where

$$\tilde{\xi}_i^{\,n+\theta} = \theta\tilde{\xi}^n + (1-\theta)\,\xi^{n+1}, \tag{36}$$

with two possible alternatives for the transposed convection term c_i,

$$c_i = \frac{3}{2}\xi_j^{n+1}\frac{\partial u_i^{\,n+1}}{\partial x_j} - \frac{1}{2}\xi_j^{n+2}\frac{\partial u_i^{\,n+2}}{\partial x_j}, \text{ or} \tag{37}$$

$$c_i = -\frac{3}{2}u_j^{n+1}\frac{\partial \xi_i^{\,n+1}}{\partial x_j} + \frac{1}{2}u_j^{n+2}\frac{\partial \xi_i^{\,n+2}}{\partial x_j}. \tag{38}$$

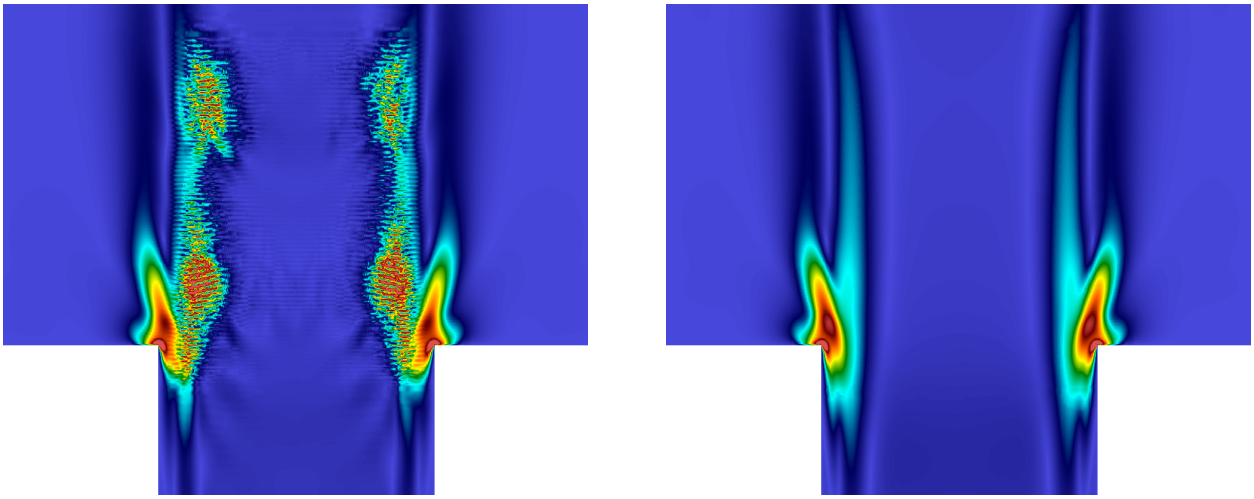

Figure 2: . Demonstration of the instability concerning the transposed convection term using a snapshot of the magnitude of the adjoint velocity $\boldsymbol{\xi}$ in the inlet region of a turbulent jet. (left): $|\boldsymbol{\xi}|$ using Eq. (38); (right): $|\boldsymbol{\xi}|$ using Eq. (37).

2. Projection step: Perform the projection ${\xi_i}^n = P({\tilde{\xi}_i}^n)$;

$$\frac{({\xi_i}^n - {\tilde{\xi}_i}^n)}{\delta t} + \frac{\partial(q^n - q^{n+1})}{\partial x_i} = 0 \quad \text{in } \Omega,$$

by solving first

$$\frac{\partial^2 (q^n - q^{n+1})}{\partial x_i \partial x_i} = \frac{1}{\delta t} \frac{\partial {\tilde{\xi}_i}^n}{\partial x_i} \quad \text{in } \Omega, \tag{39}$$

$$\frac{\partial (q^n - q^{n+1})}{\partial x_i} n_i = 0 \quad \text{on } \partial\Omega, \tag{40}$$

then, updating the velocity

$$\xi_i^n = {\tilde{\xi}_i}^n - \delta t \frac{\partial (q^n - q^{n+1})}{\partial x_i}, \quad \text{in } \Omega, \tag{41}$$

$$\xi_i^n = g_i^n \quad \text{on } \partial\Omega. \tag{42}$$

This algorithm delivers oscillatory results if the form in Eq. (38) is employed for the transposed convection term. This is demonstrated in Figure 2 by using the adjoint velocities obtained with Eq. (37) and Eq. (38) (cf. Section 5 for the problem description). We observe high-gradients around the nozzle exit for both forms. High-values of the adjoint velocity show the most sensitive areas, and we know that the jet flow is extremely sensitive to the

nozzle shape. Here we have a nozzle with sharp corners, where the adjoint velocity vanishes. As the flow is very sensitive to the shape of these corners, high values of adjoint velocity are wrapped around them, yielding high gradients. On top of this structure, the adjoint velocity obtained with the form in Eq. (38) shows a strong oscillatory behavior. Therefore, only the form in Eq. (37) is further considered in this study.

3.2. Discretization of the controls

The controls are body forces that are defined in small hexahedral regions Ω_c. The forcing is uniform in each region and is applied only in the radial direction $\boldsymbol{e}_r$. The control signals are unsteady and discretized in time by using truncated Fourier series. The control parameters to optimize are the Fourier coefficients in these Fourier series. The forcing signal of each actuator $k \in \{1, \dots, 12\}$ reads as follows

$$\boldsymbol{\phi}^h(x,t) = -\boldsymbol{e}_r^k \sum_{m=1}^{10} \alpha_{k,2m-1} \sin 2\pi n f_o t + \alpha_{k,2m} \cos 2\pi n f_o t, \quad \forall \boldsymbol{x} \in \Omega_c^k, \tag{43}$$

where f_o is the fundamental control frequency, and $\boldsymbol{\alpha} \in \mathbb{R}^K$ is the finite-dimensional control vector which contains all control variables $\alpha_{k,n}$, with $n = 1 \cdots 20$, leading to $K = 240$. Each actuator has 10 Fourier components, covering an actuation range between $f_o = 0.5\mathrm{St}_{pm}$ and $10 f_o = 5\mathrm{St}_{pm}$ where $\mathrm{St}_{pm} := \mathrm{St}_D = 0.33$ is the considered preferred mode frequency of the jet. At the low end, this actuation range is determined by the length of the optimization horizon, while at the high end, it is limited by the time step. The lowest frequency component, i.e. the one with $\mathrm{St}_D = 0.165$, has two periods in the considered optimization horizon $T = 4/\mathrm{St}_{pm}$, cf. Section 5. The highest frequency component, i.e. $\mathrm{St}_D = 1.65$, has a period resolved by 20 time steps, so that the control signal remains well resolved on the time step.

In Section 2 the gradient of the reduced cost funtional is derived using continous controls. Now this derivation is extended for the discrete controls. In order to find the gradient of the reduced cost functional with respect to Fourier coefficients $\boldsymbol{\alpha}$, we replace $\boldsymbol{\phi}$ with $\boldsymbol{\phi}^h$ in the Lagrangian $\mathcal{L}$ in Eq. (13), and take the directional derivative of the $\mathcal{L}$ with respect to an

arbitrary perturbation $\boldsymbol{\alpha}' \in \mathbb{R}^K$, such that

$$\mathcal{L}_\alpha(\alpha') = \sum_{m=1}^{K} \left(\int_0^T \gamma \alpha_m \mathrm{dt} + \int_0^{\mathrm{T}} \int_{\Omega_\mathrm{c}} \frac{\partial \phi_\mathrm{i}^\mathrm{h}}{\partial \alpha_\mathrm{m}} \xi_\mathrm{i} \mathrm{d}\boldsymbol{x}\mathrm{dt} \right) \alpha'_m, \tag{44}$$

where the derivative $\partial \boldsymbol{\phi}^h / \partial \alpha_m$ is calculated using Eq. (43) as follows

$$\frac{\partial \boldsymbol{\phi}^h}{\partial \alpha_{2m-1}} = -\boldsymbol{e}_r^k \sin 2\pi n f_o t,$$

and

$$\frac{\partial \boldsymbol{\phi}^h}{\partial \alpha_{2m}} = -\boldsymbol{e}_r^k \cos 2\pi n f_o t.$$

If we use the finite-dimensional scalar product and define the discrete reduced gradient $\nabla \tilde{\mathcal{J}}^h$ as follows

$$\left(\nabla \tilde{\mathcal{J}}^h, \boldsymbol{\alpha}' \right) = (\nabla_{\boldsymbol{\alpha}} \mathcal{L}, \boldsymbol{\alpha}') := \mathcal{L}_{\boldsymbol{\alpha}}(\boldsymbol{\alpha}') \quad \forall \boldsymbol{\alpha}' \in \mathbb{R}^K, \tag{45}$$

then we obtain

$$\nabla \tilde{\mathcal{J}}^h(\boldsymbol{\alpha}) = \int_0^T \gamma \boldsymbol{\alpha} \mathrm{dt} + \int_0^{\mathrm{T}} \int_{\Omega_\mathrm{c}} \frac{\partial \phi_\mathrm{i}^\mathrm{h}}{\partial \boldsymbol{\alpha}} \xi_\mathrm{i} \mathrm{d}\boldsymbol{x}\mathrm{dt}. \tag{46}$$

Integrals are evaluated with the midpoint rule. As only the discrete gradient will be used hereafter, we will drop the superscript h.

3.3. Computational setting

The cylindrical computational domain (cf. Figure 1a) is discretized with an O-grid type of grid. This grid is similar to the one described in Ref. [22], which was verified for first and second order turbulence statistics up to $6D$ downstream the orifice by conducting a grid assessment study on multiple grids. There are two main differences between the grid in this study and the one in Ref. [22]. Firstly, the considered domain in this study is smaller, which allows approximately three times higher overall grid density for the same number of elements. This is required mainly for the solution of adjoint equations, as the additional transposed convection term in these equations yields an adjoint flow with finer

scales compared to the primal flow. Secondly, we applied two levels of local grid refinements in the control regions. The motivation for these refinements is to resolve the adjoint fields in the control regions and provide accurate gradient information. Each level of refinement doubles the grid density in every direction. The first level of refinement is applied in the domain $\Omega_{r1} = [0, 0.8D] \times [0, 2\pi] \times [-0.2D, D]$, which is defined in the radial, azimuthal and axial directions respectively. An additional level of refinement is applied in the domain $\Omega_{r2} = [0.48D, 0.6D] \times [0, 2\pi] \times [0.025D, 0.5D]$. Overall, the computational grid consists of approximately 184×10^6 computational elements.

The primal and adjoint Navier–Stokes equations are solved with DNS. The very fine grid resolution in control regions requires a modification in the temporal discretization compared to the one employed in the DNS study in Ref. [22]. In order to keep the study feasible, we increase the implicitness parameter θ introduced in Section 3.1, to $\theta = 0.66$ for the primal DNS problem, and to $\theta = 0.9$ for the adjoint problem. This increment allowed a time step of $\delta t = 0.0303 D U_J^{-1}$, enabling us to resolve one period of actuation for the highest frequency component ($5\mathrm{St}_{pm}$) with 20 time steps.

The boundary conditions at lateral Γ_r and outflow Γ_o boundaries correspond respectively to $\partial u_i/\partial r = 0$, and $\partial u_i/\partial x = 0$ for the velocity, and in the same way, $\partial \xi_i/\partial r = 0$, and $\partial \xi_i/\partial x = 0$ for the adjoint velocity. No inflow is allowed on the outflow boundary for velocity fields. On the inlet Γ_i and pipe Γ_p boundaries, the velocity has a uniform profile in the axial direction, i.e., $u_x = U_J$, and the adjoint velocity vanishes, i.e., $\xi_i = 0$.

Initial fields for the velocity are produced by allowing an uncontrolled jet develop in the domain. The initial condition for the adjoint velocity is the zero field, cf. Eq. (27).

3.4. Verification of the adjoint-based gradient

In this section, the adjoint-based gradients are compared to finite-difference gradients for the transitional jet case at $\mathrm{Re}_D = 2000$. Both the error on the direction of the gradient, and its magnitude are verified. To this end, a subset $\boldsymbol{\alpha}_{A0} \in \mathbb{R}^{10}$ corresponding to Fourier coefficients of cosine components in the forcing region $A0$ is extracted from $\boldsymbol{\alpha} \in \mathbb{R}^K$ and the

Table 2: Comparison of adjoint and finite-difference gradients for five different time horizons T using the measure e_g in Eq. (47).

T	T_{pm}	$2T_{pm}$	$3T_{pm}$	$4T_{pm}$	$5T_{pm}$
e_g	0.0003	0.0012	0.0079	0.0078	0.0043
$\|\nabla\tilde{\mathcal{J}}_a\|/\|\nabla\tilde{\mathcal{J}}_{fd}\|$	0.9814	0.8723	0.6948	0.8344	0.7178

following error measure to quantify the accuracy of the gradient direction is introduced

$$e_g := 1 - \frac{\nabla\tilde{\mathcal{J}}_a \cdot \nabla\tilde{\mathcal{J}}_{fd}}{\|\nabla\tilde{\mathcal{J}}_a\|\|\nabla\tilde{\mathcal{J}}_{fd}\|}, \tag{47}$$

where $\nabla\tilde{\mathcal{J}}_a \in \mathbb{R}^{10}$ is the gradient of the reduced cost functional with respect to the control parameters in $\boldsymbol{\alpha}_{A0}$, which is calculated by the adjoint method with the Eq. (46), and $\nabla\tilde{\mathcal{J}}_{fd} \in \mathbb{R}^{10}$ is the finite-difference gradient calculated by

$$(\nabla\tilde{\mathcal{J}}_{fd}(\boldsymbol{\alpha}))_i := \frac{\tilde{\mathcal{J}}(\boldsymbol{\alpha} + \epsilon\boldsymbol{\delta\alpha}_i) - \tilde{\mathcal{J}}(\boldsymbol{\alpha})}{\epsilon}, \tag{48}$$

where $\boldsymbol{\delta\alpha}_i = [0, \ldots, 1, \ldots, 0]$ is the perturbation direction regarding the cosine component, and $\epsilon = 10^{-6}\alpha_i$ is selected as the magnitude of perturbation.

We evaluate the gradient for five different time horizons $T = T_{pm}, \ldots, 5T_{pm}$ at a control point $\boldsymbol{\alpha}_r$ with uniform coefficients, i.e.,

$$\boldsymbol{\alpha}_r = [0.1\mathcal{F}_0, \ldots, 0.1\mathcal{F}_0],$$

where $\mathcal{F}_0 = 1.8(U_J^2/D)$, and T_{pm} is the preferred mode period. The observation domain is described in Section 5. The calculation of e_g for each time horizon requires one primal solution for the evaluation at the reference point $\boldsymbol{\alpha}_r$, ten additional primal solutions to calculate the finite-difference gradient $\nabla\tilde{\mathcal{J}}_{fd}(\boldsymbol{\alpha}_r)$ and one adjoint solution to compute $\nabla\tilde{\mathcal{J}}_a(\boldsymbol{\alpha}_r)$. Therefore, this verification study covering five different time horizons requires 60 PDE solutions in total.

The direction of the adjoint gradients are in very good alignment with the direction of the finite-difference gradients. However, the magnitude of the adjoint gradient is not matching

the finite-difference gradient so well. These differences may be caused by both spatial and temporal discretization errors, as well as differences in boundary conditions (cf. discussion in Section 2.3). In particular, the high implicitness parameter ($\theta = 0.9$), employed in the temporal discretization of the adjoint equations introduces numerical diffusion, and an error that is first order in time. The need for this numerical diffusion is related to the challenging nature of the adjoint solution itself as discussed in detail in Section 4.

Given the high computational costs of the simulations, we cannot simply further refine grid or time steps to verify this, and reduce the error between forward and adjoint gradient. Therefore, we will continue the optimization in Section 5 using the strong working assumption that $\nabla\tilde{\mathcal{J}}_a \sim \nabla\tilde{\mathcal{J}}_{fd}$, i.e. we presume that the direction of the gradient is sufficiently accurate to be used in a steepest-descent method. Note that steepest-descent methods (as well as conjugate-gradient methods) mainly require a correct descent direction. The line-search in that search direction is based on the forward equations. There is a dependence on the magnitude of the gradient in the stopping criterion of the line-search (cf. Algorithm 1), but this involves a free-to-choose proportionality parameter β ($= 10^{-4}$ in our implementation), so that $\nabla\tilde{\mathcal{J}}_a \sim \nabla\tilde{\mathcal{J}}_{fd}$ may suffice. Finally, in view of computational expenses, we only consider a limited number of iterations, so that formal convergence, requiring more precise gradient evaluations, is not reached in any case (cf. Section 5). During the considered optimization cases, we did not encounter a non-descent direction, nor did we reach convergence ($\nabla\tilde{\mathcal{J}}_a = 0$) in any of the iterations.

4. Limitations concerning the adjoint-based gradient

There are two fundamental methodological issues concerning the adjoint-based calculation of the gradient when it is applied to turbulent jets. The first issue is related to the chaotic character of the turbulent flows, i.e., extreme sensitivity to initial conditions, causing a blow-up in the magnitude of the adjoint fields. Lea et al. [39] demonstrated this problem using a simplified chaotic case: a Lorentz system. They claimed that the adjoint method was a limited utility to calculate the sensitivity of time-averaged properties of the system.

In their analysis, they used different integration time windows that are referred to as intermediate, long and very long. Intermediate integration completes a full orbit around the Lorenz attractor, long integration allows the completion of several of such orbits and very long integrations travel around the attractor many times, e.g. $O(100)$. The adjoint results for intermediate and long integrations were approaching direct sensitivity results over much of the parameter range but they were still extremely inaccurate for certain values. In general, a reasonable estimation with an error of $O(10\%)$ is obtained. The adjoint method delivered completely useless gradient, with order of magnitude values around 10^{100} for very long time integrations. They concluded that there is a cumulative error growth due to one of the system's unstable modes with positive Lyapunov exponent, which causes this exponential divergence.

We observed similar issues in the turbulent round jet case. If the optimization time window is long enough to allow many through-flow times, e.g. $O(10)$ through-flow times in a domain with a length of $10D$, then the adjoint fields diverge and reach extremely high values. If we limit the time horizon, and just let the initial jet develop throughout the domain, then adjoint fields with reasonable magnitudes are obtained. This cumulative error growth while integrating backwards in time is also observed by Marinc and Foysi in the plane-jet optimization case [9], and similar problems for other test cases were reported in Refs. [40, 41]. Very recently, Wang et al. proposed a Least-Squares Shadowing method to overcome this issue [42, 43]. The method is based on approximating the shadow trajectory in phase space, and preventing the high sensitivity to the initial conditions. This approach is very new, and still requires a lot of research, and therefore falls outside of the scope of the current work.

The second issue concerning the adjoint methodology is related to the noise-amplifier character of the round jets, which causes an extremely non-uniform distribution in the adjoint velocity fields. In noise-amplifier flows, there are no intrinsic global instabilities in the flow, but the perturbations grow downstream as the result of convective instabilities [44]. The overall dynamics are therefore extrinsic and the flow acts like a fine-tuned amplifier

to perturbations [45]. Thus, the flow is extremely sensitive to upstream perturbations, and even perturbations with very small amplitudes can alter global flow states. This extremely sensitive character results in the adjoint velocity fields that are exponentially growing while moving towards the jet inlet. Thus, the adjoint-jet problem has completely different nature than the forward jet problem. In the forward problem, the nonlinearity is dominant and the exponential growth of perturbations can be seen only in initial parts of the shear layer.

As the amplification mechanisms originate from the jet shear layer, very high adjoint velocity values concentrate in this small region. Moreover, the controls are usually placed also in this region, and the gradient of the cost functional has to be computed from the adjoint fields here. Therefore, accurate computation of the gradient becomes an extremely challenging numerical problem. In general, a computational grid merely designed to solve the forward DNS, or LES, problem will fail to resolve the adjoint velocity in the shear layer and eventually compute erroneous gradients for the optimization loop.

Both issues discussed in this section, originate from the extreme sensitivity of the jet to perturbations: in time due to the chaotic character of turbulence, and in space due to the noise-amplifier character of jet flows. Therefore, optimization in a long jet domain over a long time horizon is conceptually not possible. This is illustrated with a 2D Bickley jet example. In this example, a jet enters a large 2D domain through a 2D channel with a width of D. The Reynolds number $\mathrm{Re}_D = 800$. Controls are two oscillatory velocity boundary conditions that are located at each side of the jet inlet (cf. Figure 3a). A cost functional measuring the enstrophy in an observation domain $\Omega_s := [-20D, 20D] \times [5D, 100D]$ over a time horizon T of 10 through-flow times is selected.

A planar computational domain extending up to $120D$ downstream the jet inlet and up to $30D$ from the jet centreline is built. Additionally, a 2D channel with a length $30D$ is attached to the large domain. The computational domain is discretized with approximately 4.3×10^6 quadrilateral elements. In order to solve the primal and adjoint Navier–Stokes equations, the incremental projection scheme is employed. The time step is selected to be $0.0001U_J/D$ where U_J is the uniform velocity at the pipe inlet.

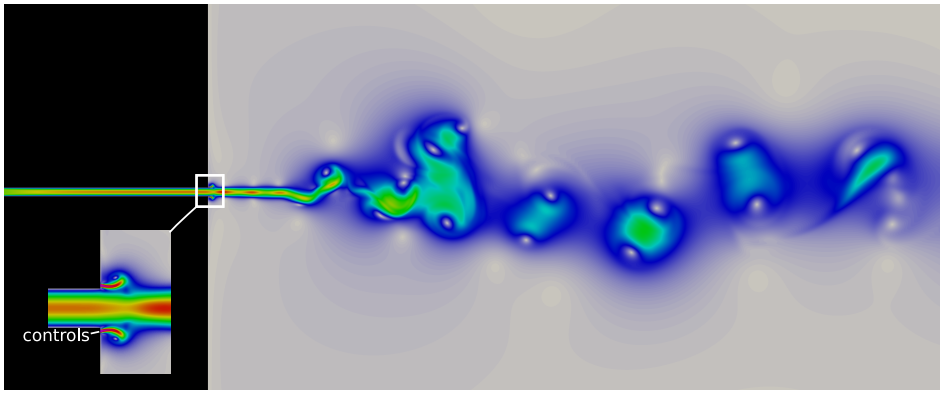

(a) Magnitude of the velocity

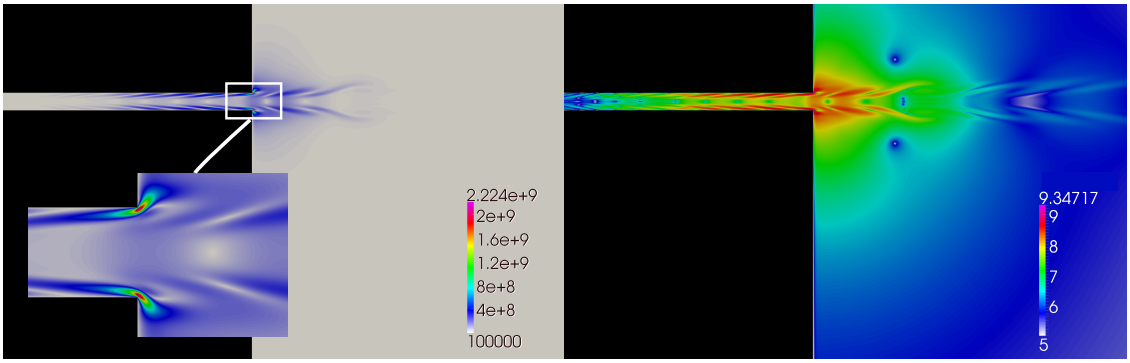

(b) Magnitude of the adjoint velocity; colormap in (left): linear scale (right): logarithmic scale

Figure 3: Exponential growth of adjoint velocity fields in the 2D Bickley jet case.

The resulting adjoint velocity fields are illustrated in Figure 3b using a time instance $t = 0.2T$. We observe that the adjoint fields grow exponentially in space towards to the jet inlet. They also grow exponentially in time while stepping backwards in time (not shown here). As a result, in the regions, where the controls are placed, the adjoint velocity field reaches up to the values of $O(10^{10})$.

5. Optimization of the distributed controls

In this section, the results of the optimization study are presented. The aim is to maximize the enstrophy measured in an observation domain Ω_s over a time window $T = (0, T]$. The cost functional with a penalization on controls is given in Eq. (3). As discussed in Sec-

Table 3: Initial conditions for two optimization cases. Case *OC2* has additional random forcing components that are not shown here, see the text for the description.

Case	*A0*	*A4*	*A8*
OC1	$\mathcal{F}_0 \cos(2\pi \mathrm{St}_{pm} t)$	$\mathcal{F}_0 \cos(2\pi \mathrm{St}_{pm} t)$	$\mathcal{F}_0 \cos(2\pi \mathrm{St}_{pm} t)$
OC2	$\mathcal{F}_0 \cos(2\pi (2\mathrm{St}_{pm}) t)$	$\mathcal{F}_0 \cos(2\pi (2\mathrm{St}_{pm}) t)$	$\mathcal{F}_0 \cos(2\pi (2\mathrm{St}_{pm}) t)$

Table 4: Summary of optimization results. The subscript 0 and f denote the values at initial and final iterations respectively.

Case	# outer iterations	$\tilde{\mathcal{J}}_f/\tilde{\mathcal{J}}_0$	$\|\boldsymbol{\alpha}_f\|/\|\boldsymbol{\alpha}_0\|$
OC1	18	1.1049	1.0038
OC2	9	1.0560	1.0317

tion 2.1, the observation domain Ω_s is selected to be $\Omega_s = [0, 5D] \times [0, 2\pi] \times [0.6D, 6D]$, in the radial, azimuthal and axial directions respectively. The optimization horizon $T = 4T_{pm}$. This value of T requires the storage of 400 velocity time steps, which occupy an overall storage space of approximately 4 terabytes. The simulations are run using 200 processors on the *Thinking* cluster of Flemish Supercomputer Center (VSC). A primal solution lasts approximately 12 hours, and an adjoint solution lasts approximately 15 hours.

Since gradient-based methods are known to converge to local optima (cf. e.g. [8]), two optimization cases with different initial conditions are considered. These cases are presented in Table 3. In the Case *OC1*, the initial condition is inspired from the Case *C1* in Ref. [22], i.e, only three actuators, *A0*, *A4*, *A8*, are active and are driven in phase with the preferred mode frequency St_{pm}. The magnitude of the actuation is $\mathcal{F}_0 = 1.8(U_J^2/D)$. This forcing magnitude is found to deliver a radial perturbation of the velocity reaching up to the values comparable to the jet exit velocity U_J. In the second case, i.e. Case *OC2*, the same actuator configuration with different control frequency, i.e. $2\mathrm{St}_{pm}$, is considered. Additionally, for this case we superimposed a random component with a maximum magnitude of $0.005\mathcal{F}_0$ on every element of the forcing vector $\boldsymbol{\alpha}$.

The optimization results are summarized in Table 4 and illustrated in Figure 4 using normalized cost functionals and norm of the gradients. For both cases, the decrease in the cost functional slows down after a few iterations. We observed that (not shown here) each outer iteration corresponds on average to approximately 4 PDE solutions with DNS, where a PDE solution requires around 2500 CPU hours, as described above. Therefore, optimizations are stopped if a minimum reduction of around 5% is obtained and relative improvements in the cost functional at each outer iteration are found not cost-efficient. For Case *OC1*, a reduction of 10.5% is observed after 18 outer iterations. The norm of the gradient decreases from $\nabla\tilde{\mathcal{J}} \approx 1.2$ to $\nabla\tilde{\mathcal{J}} \approx 0.6$ showing that the local minimum is not reached yet. In the Case *OC2*, the cost functional is reduced around 5.6% after 9 outer iterations. In the final outer iteration, $\nabla\tilde{\mathcal{J}} \approx 0.4$, again showing that the local optimum is still not reached.

The relative reduction in the cost functional of Case *OC2* is lower compared to the one of Case *OC1*. Furthermore, this limited reduction is achieved by increasing the norm of the controls more than 3% where this increase is only 0.3% in Case *OC1* (cf. Table 4). This result suggests that the addition of a random component on the controls makes the problem more challenging for the optimizer. On the other hand, the final value of $\tilde{\mathcal{J}}$ in Case *OC2* is 10% less than the one of Case *OC1* thanks to the more efficient initialization, i.e., initialization with the double of the preferred mode increases the global sum of enstrophy more efficiently than the initialization with the preferred mode. This is in qualitative agreement with the discussion in Section 1, where actuation with the preferred mode is claimed to be stabilizing the larger scales, and therefore inefficient for the smaller scale transition.

The resulting optimized control signals are first converted into the phase angle form, such that

$$\overline{\alpha}_n \cos(2\pi(nf_o)t + \varphi_n) = \alpha_{2n-1} \sin(2\pi(nf_o)t) + \alpha_{2n} \cos(2\pi(nf_o)t), \tag{49}$$

and plotted subsequently on the polar axes $r = \overline{\alpha}_n/\mathcal{F}_0$ and $\theta = \varphi_n$ in Figure 5 and 6. Control regions that are $2\pi/3$ away from each other in the azimuthal direction, are plotted together, as their signals exhibit similar distributions.

The signals of the initially active forcing regions, i.e., *A0*, *A4*, *A8*, remain approximately

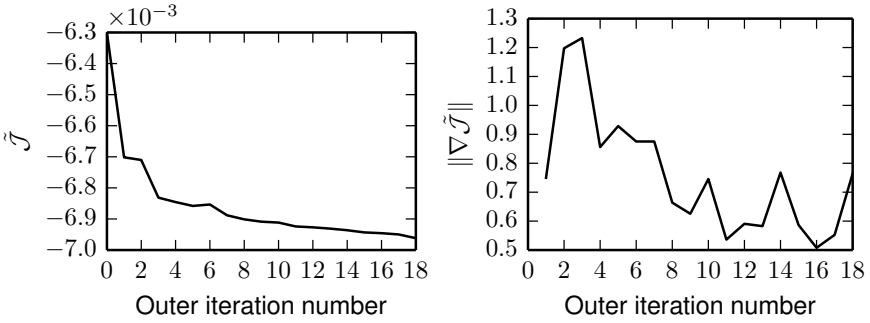

(a) Case *OC1* (b) Case *OC1*

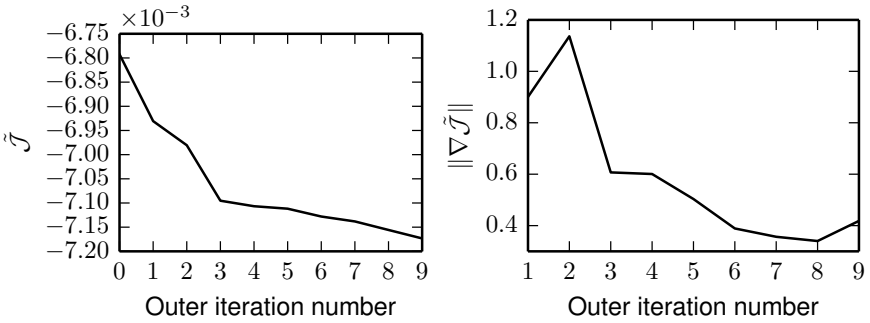

(c) Case *OC2* (d) Case *OC2*

Figure 4: Optimization results for Cases *OC1* and *OC2*. (a),(c): cost functional; (b),(d): norm of the reduced gradient,

unchanged after optimization, as we can see in Figure 5a and 6a. The optimized amplitudes in other regions remain in low magnitude compared to the initial forcing $\mathcal{F}_0$. Especially the neighbouring regions to *A0*, *A4*, *A8*, i.e., *A1*, *A5*, *A9* and *A3*, *A7*, *A11*, have the lowest energy content for both optimization cases, cf. Figure 5b,d and 6b,d. For these regions, the amplitudes of frequency components remains approximately below $0.02\mathcal{F}_0$ for Case *OC1* and $0.04\mathcal{F}_0$ for Case *OC2*. Moreover, there are no obvious trends in the distribution of phase angles. In contrast, for forcing regions *A2*, *A6*, *A10* in Figure 5c and 6c, phase angle values concentrate in the region $-\pi/4 < \theta + \pi < \pi/4$, which suggests a $\varphi_n \approx \pi$ out-of-phase behaviour with respect to the initially active actuators *A0*, *A4*, *A8*. Moreover, forcing in these regions, is more pronounced compared to regions neighbouring them. In Case *OC1*, the most amplified frequency component is $2\mathrm{St}_{pm}$ for the actuators *A2*, *A6*, *A10*, and its amplitude corresponds to approximately $0.04\mathcal{F}_0$ (cf. dashed circles in Figure 5c). Furthermore, the most amplified frequency component in Case *OC2* is $3\mathrm{St}_{pm}$ for the actuators *A2*, *A6*, *A10*, and with an amplitude that corresponds to approximately $0.08\mathcal{F}_0$ (cf. dashed circles in Figure 6c).

Figure 7 presents streamwise snapshots of $|\boldsymbol{\omega}|$ in Case *OC2* for initial and final optimized controls in the forcing plane of *A0*, i.e. a cutplane passing through the centroid of *A0*. Furthermore, Figure 8 illustrates the instantaneous snapshots of $|\boldsymbol{\omega}|$ on various cross-section planes. We observe that the distributed actuation is able to produce some characteristic primary and secondary vortex features of ZNMF actuated jets. At $x = D$, we see the cross section of a tilted vortex ring, which is marked with a solid line Figure 7a. These asymmetric rings are typical for flows that lose their axisymmetry due to cross-stream perturbations, as discussed in Refs. [26, 22]. This primary vortex ring is unaffected by optimization and develops approximately with the same structure in the unoptimized flow as in the optimized flow (cf .Figure 7a and Figure 7b).

Looking further at the forcing plane of *A0* in Figure 7a, we note the presence of a streamwise vortex filament in the unoptimized flow (cf. dashed line). These secondary structures are first formed between the peak sides of primary rings (cf. Refs. [26, 22] for

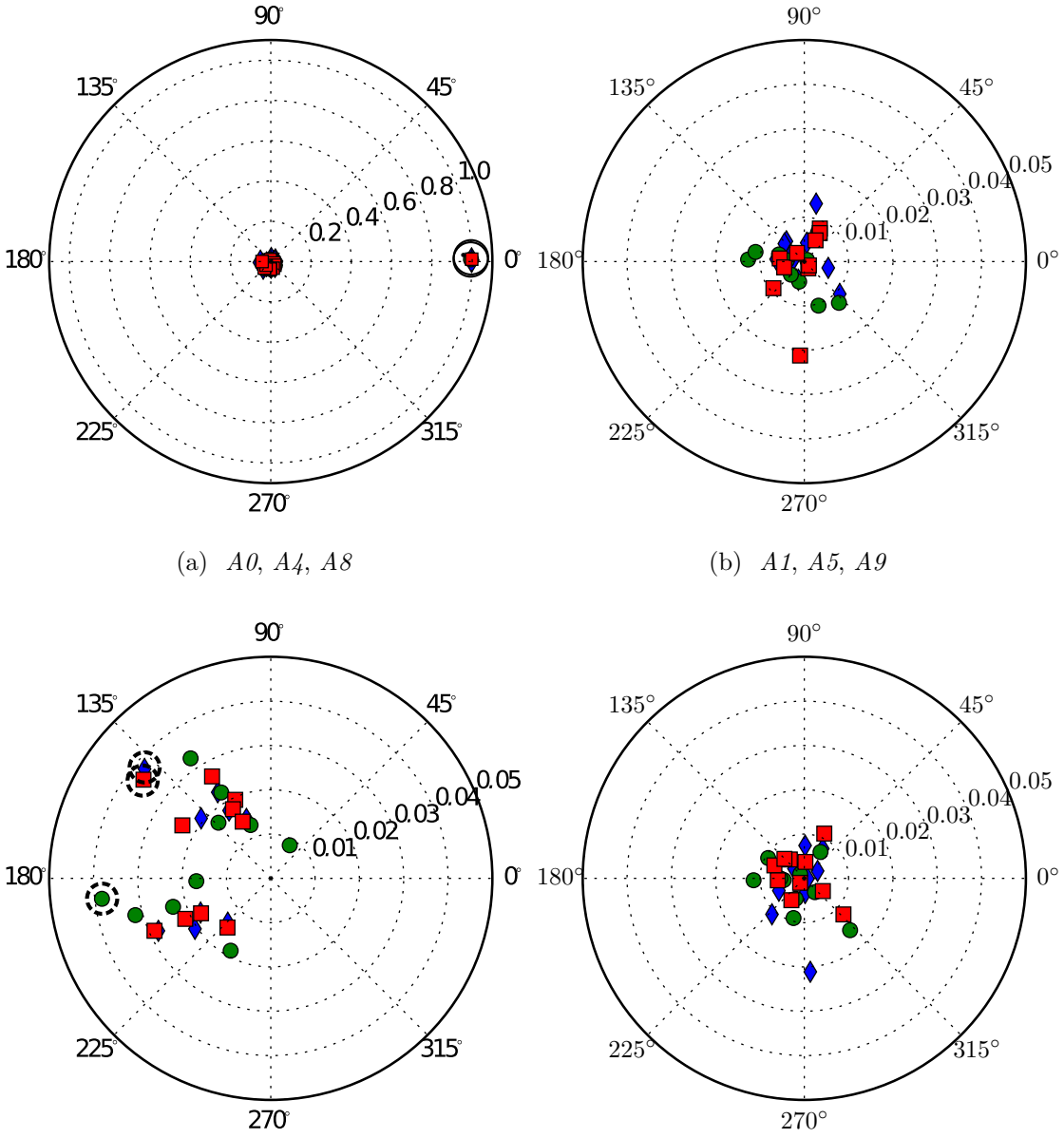

(a) *A0*, *A4*, *A8*

(b) *A1*, *A5*, *A9*

(c) *A2*, *A6*, *A10*

(d) *A3*, *A7*, *A11*

Figure 5: Optimized controls for Case *OC1* using a polar graph with axes $r = \overline{\alpha}_n/\mathcal{F}_0$ and $\theta = \varphi_n$. ($\diamond$): regions *A0*, *A1*, *A2*, *A3*; ($\circ$): *A4*, *A5*, *A6*, *A7*; ($\square$): *A8*, *A9*, *A10*, *A11*. The frequency information is not given. Only the frequency components with higher amplitude of forcing are marked by circles of (—): St_{pm} in (a); (−−): $2\mathrm{St}_{pm}$ in (c).

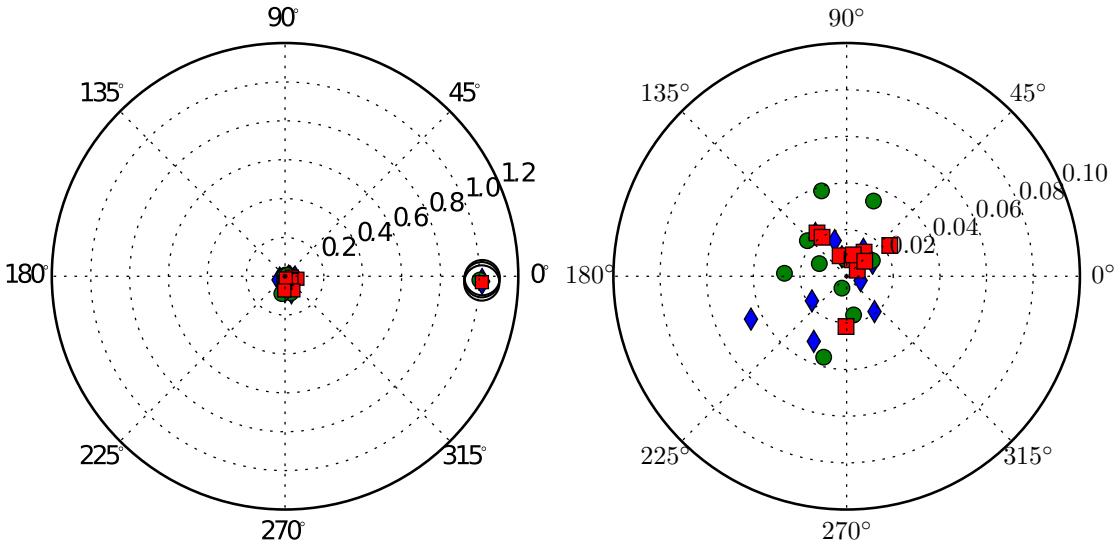

(a) *A0*, *A4*, *A8* (b) *A1*, *A5*, *A9*

(c) *A2*, *A6*, *A10* (d) *A3*, *A7*, *A11*

Figure 6: Distribution of the optimized controls for Case *OC2* using a polar graph with axes $r = \overline{\alpha}_n/\mathcal{F}_0$ and $\theta = \varphi_n$. See Figure 5 for captions. The frequency components with higher amplitude of forcing are marked by circles of (—): $2\mathrm{St}_{pm}$ in (a); (−−): $3\mathrm{St}_{pm}$ in (c).

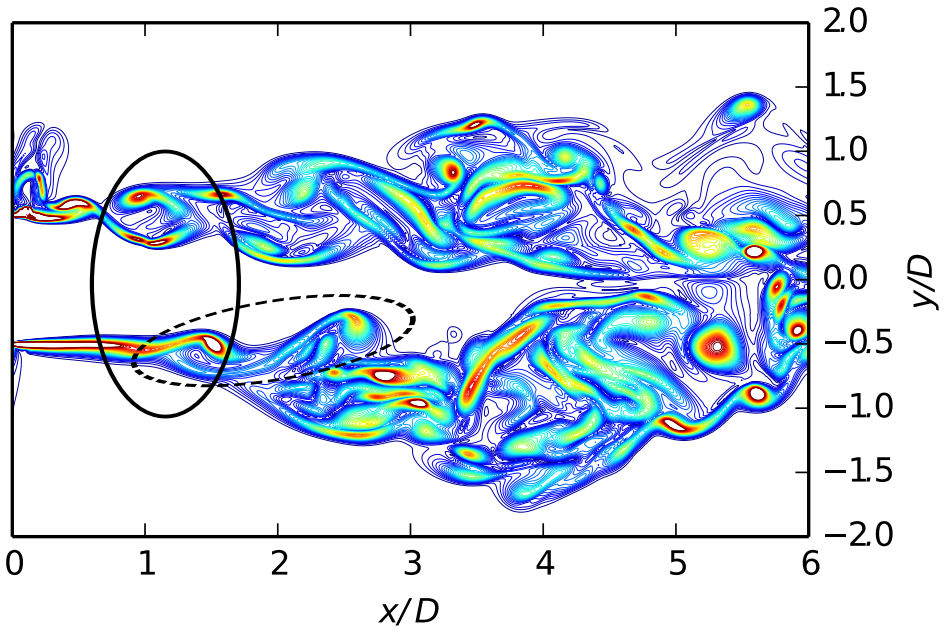

(a) iteration=0

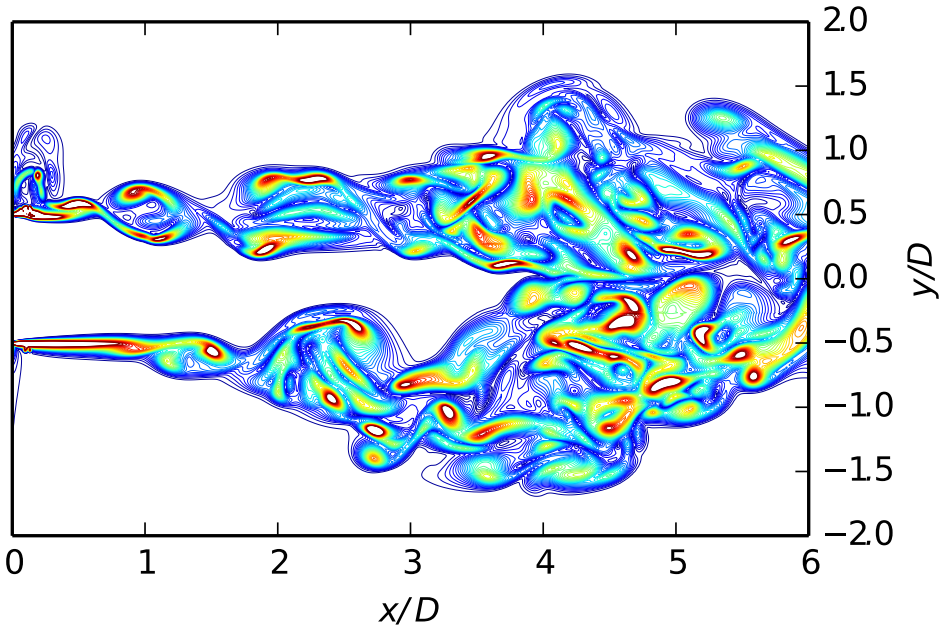

(b) iteration=9

Figure 7: Instantaneous snapshots of $|\boldsymbol{\omega}|$ at $t = 4T_{pm}$ on the forcing plane of *A0* for unoptimized (a) and optimized (b) jet flows in Case *OC2*.

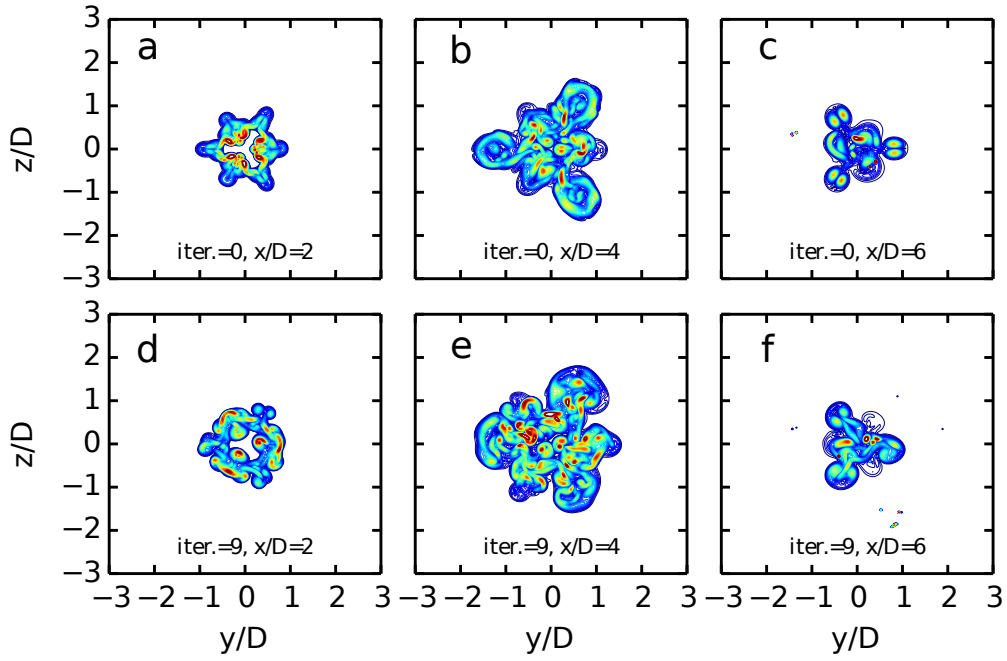

Figure 8: Instantaneous snapshots of $|\boldsymbol{\omega}|$ at $t = 4T_{pm}$ on various cross-section planes for unoptimized (a, b, c) and optimized (d, e, f) jet flows in Case *OC2*.

a detailed discussion). A secondary structure is also evident in the optimized flow but somewhat less organized (see Figure 7b). This can be seen more clearly on the cross-section plane at $x/D = 2$ in Figure 8. For the unoptimized flow, a very regular characteristic hexagram pattern, which is produced by tilted vortex rings and streamwise vortex filaments, can be seen in Figure 8a. The same pattern appears also in the optimized flow but in a somewhat perturbed fashion (cf. Figure 8d). The differences between optimized and unoptimized flows increase moving downstream, as we can see on cutplanes at $x/D = 4$ in Figures 8b and 8e. The optimized jet develops the characteristic pattern of an azimuthally perturbed jet but has much more irregularity and has more vorticity content. At $x/D = 6$ in Figures 8c and 8f, we see three streamwise vortex pairs in a braid region, which are located at the corners of triangular patterns.

6. Conclusions

In this work, an optimal control study for an axisymmetric jet at $\mathrm{Re}_D = 2000$ was performed. The optimization method of choice was a steepest descent method where the gradient is calculated with the continuous adjoint method. In contrast to common practise with the continous adjoint method in the flow optimization community, we derived adjoint boundary conditions using only Dirichlet boundaries, as computational Neumann boundary conditions in the primal problem are considered unphysical. Such a strategy avoided complicated adjoint boundary conditions originating from the Neumann boundary conditions. Instead, we employed simple Neumann boundary conditions also for the adjoint velocity on the computational boundaries.

A new unsteady solver to solve the adjoint equations is implemented into OpenFOAM®. The solver is based on the adjoint version of the incremental projection scheme. In this algorithm, the additional transposed convection term is treated with Adams-Bashfort method, as OpenFOAM® does not support the implicit treatment of coupled velocity terms. It was found that this form $-u_j \partial \xi_j / \partial x_i$ of transposed convection term delivers unstable results, and instead, the form $\xi_j \partial u_j / \partial x_i$ was used.

Using a 2D Bickley jet example, it was demonstrated that the adjoint method fails to provide gradient information in long time horizons. This problem originates from the extreme sensitivity of the jet to perturbations: in time due to the chaotic character of turbulence, and in space due to the noise-amplifier character of jet flows. Therefore, optimization in a long jet domain over a long time horizon was conceptually not possible with adjoint methodology. Consequently, we performed an optimization study for an observation domain extending only up to $6D$ in streamwise direction and limited the optimization horizon to the time interval where the jet transient develops. These selections were also motivated by computational restrictions such as the storage space and the turnaround time.

The controls in the jet-optimization study were modelled as twelve small hexahedral regions around the jet circumference with a uniform forcing distribution. Forcing was applied only in the radial direction. The signal of controls was designed as a finite Fourier series with 10 frequency components varying between $0.5\mathrm{St}_{pm}$ and $5\mathrm{St}_{pm}$. Optimization was carried out for these Fourier coefficients in the Fourier series, yielding a total size of 240 for the control space. Two different initial conditions, referred to as Case *OC1* and Case *OC2*, were considered for optimization. These initial controls were inspired from Case *C1* and Case *C2* in Ref. [22], where three actuators were driven in phase with a frequency of St_{pm} and $2\mathrm{St}_{pm}$ respectively. For Case *OC2*, an additional random component with a low amplitude was added on every element of the control vector.

The accuracy of the adjoint-based gradient was verified by performing a comparative study using finite-difference based gradients. The gradients were evaluated only with respect to the Fourier coefficients of cosine components in the actuator *A0*. The tests were run for five different optimization horizons and required 60 PDE solutions in total. We found that the directions of the adjoint-based and finite-difference gradients were in good agreement, but their magnitudes were not. This is possibly caused by discretization errors in space as well as in time. In particular, to keep time integration of the adjoint equations stable, we had to use a high implicitness parameter ($\theta = 0.9$), which introduces a difference that is first order in time. Computational resources did not allow us to further refine grid or

time steps, and instead we continued optimization using the working assumption that the adjoint gradients provide sufficient directional information to perform optimization using a steepest-descent method.

Optimizations were conducted, and reductions of 10.5% and 5.6% were observed for Case *OC1* and Case *OC2* respectively. Optimizations were stopped prematurely for resource reasons, before local optima were formally reached. The relative reduction in Case *OC2* was lower compared to the one of Case *OC1*. Furthermore, this limited reduction was achieved by increasing the magnitude of controls more than for Case *OC1*. We believe that this was due to the fact that the addition of a random component on the controls made the problem more challenging for the optimizer. The final value of enstrophy in Case *OC2* was 10% higher than the one of Case *OC1* thanks to the more efficient initialization with $2\mathrm{St}_{pm}$.

Finally, the optimized signals and fields were discussed. Modifications were analysed, where low energy modifications (less than 10% of the initial forcing amplitude) were observed in forcing amplitudes of initially passive actuators. These low-amplitude changes in controls were capable of altering the evolution of the jets downstream as demonstrated by the snapshots of vorticity fields in Case *OC2*. In the optimized flow, primary and secondary vortex features were more unstable compared to the ones in unoptimized flow, and therefore the typical geometric patterns in jet-cross sections were more irregular.

Acknowledgements

The authors acknowledge financial support by the KU Leuven research council (BOF, special research fund, grant number OT/08/029). Simulations were performed on the *Thinking* computing infrastructure of the VSC Flemish Supercomputer Center, funded by the Hercules Foundation and the Flemish Government.

References

[1] S. C. Crow, F. H. Champagne, Orderly structure in jet turbulence, Journal of Fluid Mechanics 48 (1971) 547–591.

[2] G. L. Brown, A. Roshko, On density effects and large structure in turbulent mixing layers, Journal of Fluid Mechanics 64 (1974) 775–816.

[3] R. D. Joslin, D. N. Miller, Fundamentals and applications of modern flow control, American Institute of Aeronautics and Astronautics, 2009.

[4] S. Walther, C. Airiau, A. Bottaro, Optimal control of tollmien–schlichting waves in a developing boundary layer, Physics of Fluids (1994-present) 13 (7) (2001) 2087–2096.

[5] C. Airiau, A. Bottaro, S. Walther, D. Legendre, A methodology for optimal laminar flow control: Application to the damping of tollmien–schlichting waves in a boundary layer, Physics of Fluids (1994-present) 15 (5) (2003) 1131–1145.

[6] T. R. Bewley, P. Moin, R. Temam, DNS-based predictive control of turbulence: an optimal benchmark for feedback algorithms, Journal of Fluid Mechanics 447 (2001) 179–225.

[7] M. Wei, J. B. Freund, A noise-controlled free shear flow, Journal of Fluid Mechanics 546 (2006) 123–152.

[8] S. Delport, M. Baelmans, J. Meyers, Maximizing dissipation in a turbulent shear flow by optimal control of its initial state, Physics of Fluids 23 (4) (2011) 045105.

[9] D. Marinc, H. Foysi, Investigation of a continuous adjoint-based optimization procedure for aeroacoustic control of plane jets, International Journal of Heat and Fluid Flow 38 (2012) 200–212.

[10] J. Schulze, P. Schmid, J. Sesterhenn, Iterative optimization based on an objective functional in frequency-space with application to jet-noise cancellation, Journal of Computational Physics 230 (15) (2011) 6075 – 6098.

[11] J. Kim, D. J. Bodony, J. B. Freund, Adjoint-based control of loud events in a turbulent jet, Journal of Fluid Mechanics 741 (2014) 28–59.

[12] C. Othmer, A continuous adjoint formulation for the computation of topological and surface sensitivities of ducted flows, International Journal for Numerical Methods in Fluids 58 (8) (2008) 861–877.

[13] C. S. Andreasen, A. R. Gersborg, O. Sigmund, Topology optimization of microfluidic mixers, International Journal for Numerical Methods in Fluids 61 (5) (2009) 498–513.

[14] A. Zymaris, D. Papadimitriou, K. Giannakoglou, C. Othmer, Continuous adjoint approach to the spalart–allmaras turbulence model for incompressible flows, Computers & Fluids 38 (8) (2009) 1528–1538.

[15] A. Stück, T. Rung, Adjoint rans with filtered shape derivatives for hydrodynamic optimisation, Computers & Fluids 47 (1) (2011) 22–32.

[16] E. Kontoleontos, E. Papoutsis-Kiachagias, A. Zymaris, D. Papadimitriou, K. Giannakoglou, Adjoint-based constrained topology optimization for viscous flows, including heat transfer, Engineering Optimization 45 (8) (2013) 941–961.

[17] A. Carnarius, F. Thiele, E. Özkaya, A. Nemili, N. R. Gauger, Optimal control of unsteady flows using a discrete and a continuous adjoint approach, in: System Modeling and Optimization, Springer, 2013, pp. 318–327.

[18] S. Delport, M. Baelmans, J. Meyers, Constrained optimization of turbulent mixing-layer evolution, Journal of Turbulence 10 (2009) 18.

[19] K. Toyoda, R. Hiramoto, Manipulation of vortex rings for flow control, Fluid Dynamics Research 41 (5) (2009) 051402.

[20] M. Samimy, J. Kim, J. Kastner, I. Adamovich, Y. Utkin, Active control of high-speed and high-Reynolds-number jets using plasma actuators, Journal of Fluid Mechanics 578 (1) (2007) 305–30.

[21] D. A. Tamburello, M. Amitay, Active control of a free jet using a synthetic jet, International Journal of Heat and Fluid Flow 29 (4) (2008) 967 – 984.

[22] A. Önder, J. Meyers, Modification of vortex dynamics and transport properties of transitional axisymmetric jets using zero-net-mass-flux actuation, Physics of Fluids 26 (7) (2014) 075103.

[23] G. Nathan, J. Mi, Z. Alwahabi, G. Newbold, D. Nobes, Impacts of a jet's exit flow pattern on mixing and combustion performance, Progress in Energy and Combustion Science 32 (56) (2006) 496 – 538.

[24] A. Hilgers, B. Boersma, Optimization of turbulent jet mixing, Fluid Dynamics Research 29 (6) (2001) 345–368.

[25] H. Suzuki, N. Kasagi, Y. Suzuki, Active control of an axisymmetric jet with distributed electromagnetic flap actuators, Experiments in Fluids 36 (3) (2004) 498–509.

[26] P. Brancher, J. Chomaz, P. Huerre, Direct numerical simulations of round jets: vortex induction and side jets, Physics of Fluids 6 (5) (1994) 1768–1774.

[27] A. Tsinober, An informal introduction to turbulence, Springer, 2001.

[28] J. M. Ottino, The kinematics of mixing: stretching, chaos, and transport, Cambridge University Press, 1994.

[29] H. Choi, M. Hinze, K. Kunisch, Instantaneous control of backward-facing step flows, Applied Numerical Mathematics 31 (2) (1999) 133–158.

[30] M. Gunzburger, Perspectives in Flow Control and Optimization, Society for Industrial and Applied Mathematics, 2002.

[31] A. Borz, V. Schulz, Computational optimization of systems governed by partial differential equations, Vol. 8, SIAM, 2012.

[32] F. Tröltzsch, Optimal control of partial differential equations: theory, methods, and applications, Vol. 112, American Mathematical Soc., 2010.

[33] J. P. Goit, J. Meyers, Analysis of turbulent flow properties and energy fluxes in optimally controlled wind-farm boundary layers, in: Journal of Physics: Conference Series, Vol. 524, IOP Publishing, 2014, p. 012178.

[34] A. Önder, Active control of turbulent axisymmetric jets using zero-net-mass-flux actuation, Ph.D. thesis, KU Leuven (2014).

[35] M. Hinze, R. Pinnau, M. Ulbrich, S. Ulbrich, Optimization with PDE constraints, Springer, New York, 2009.

[36] C. T. Kelley, Iterative methods for optimization, Vol. 18, Siam, 1999.

[37] H. Jasak, Error analysis and estimation for the finite volume method with applications to fluid flows, Ph.D. thesis, Imperial College London (University of London) (1996).

[38] J. van Kan, A second-order accurate pressure correction scheme for viscous incompressible flow, SIAM J. Sci. Stat. Comput. 7 (3) (1986) 870–891.

[39] D. J. Lea, M. R. Allen, T. W. N. Haine, Sensitivity analysis of the climate of a chaotic system, Tellus A 52 (5) (2000) 523–532.

[40] Q. Wang, J.-H. Gao, The drag-adjoint field of a circular cylinder wake at reynolds numbers 20, 100 and 500, Journal of Fluid Mechanics 730 (2013) 145–161.

[41] C. C. Pringle, A. P. Willis, R. R. Kerswell, Minimal seeds for shear flow turbulence: using nonlinear transient growth to touch the edge of chaos, Journal of Fluid Mechanics 702 (2012) 415–443.

[42] Q. Wang, R. Hu, P. Blonigan, Least squares shadowing sensitivity analysis of chaotic limit cycle oscillations, Journal of Computational Physics 267 (2014) 210–224.

[43] P. Blonigan, S. Gomez, Q. Wang, Least squares shadowing for sensitivity analysis of turbulent fluid flows, arXiv preprint arXiv:1401.4163.

[44] P. Huerre, M. Rossi, Hydrodynamic instabilities in open flows, in: C. Godrèche, P. Manneville (Eds.), Hydrodynamics and Nonlinear Instabilities, Cambridge University Press, 1998, pp. 81–294.

[45] C.-M. Ho, P. Huerre, Perturbed free shear layers, Annual Review of Fluid Mechanics 16 (1) (1984) 365–422.